Available online at www.sciencedirect.com

Thin Solid Films 496 (2006) 505 – 514

www.elsevier.com/locate/tsf

Effective optical properties of non-absorbing nanoporous thin films

Matthew M. Braun *, Laurent Pilon

Mechanical and Aerospace Engineering Department, Henri Samueli School of Engineering and Applied Science, University of California,
420 Westwood Plaza, 37-132 Eng. IV, Los Angeles, CA 90095, USA

Received 15 December 2004; received in revised form 25 July 2005; accepted 12 August 2005

Abstract

Numerous effective medium models have been proposed for the effective optical properties of nanoporous media. However, validations of these models against experimental data are often contradictory and inconclusive. This issue was numerically investigated by solving the two-dimensional Maxwell's equations in non-absorbing nanoporous thin films with various morphologies. It was found that below a certain critical film thickness, the effective index of refraction depends on the porosity and on the pore size, shape and spatial distribution. For thick enough films the effective index of refraction depends solely on porosity and on the indices of refraction of the two constitutive phases. The numerical results agree very well with a recent model obtained by applying the Volume Averaging Theory to the Maxwell's equations. However, commonly used models systematically and sometimes significantly underpredict the numerical results.

PACS: 95; 311; 345; 347
Keywords: Dielectric constant; Nanostructure; Optical properties; Optoelectronic devices

1. Introduction

Nanoporous materials consist of nanosize air pockets embedded in a solid matrix. The pores can assume different shapes and sizes and can be closed or open (i.e. connected). Nanoporous media are characterized by their bubble size distribution and porosity which can significantly affect their electrical, thermal, radiation, and optical properties. Progress in synthesizing, characterizing, and modelling such materials would enable technological innovations in various applications ranging from microelectronics to optical devices and biosensors.

As integrated circuit process technology progresses, the device density increases and chip performance improves continuously [1]. The signal propagation is delayed by the resistance–capacitance time constant RC. The resistance R has been reduced by replacing Al–Cu alloy by Cu metal lines. Further reduction can be achieved via minimizing the capacitance C. This can be accomplished by replacing the current circuit interconnect material, silicon dioxide ($\epsilon_r = 3.9$ at 1 MHz), with new low-k dielectric materials having dielectric constant ϵ_r less than 2.0. Unfortunately, there are no known dense materials that meet the semiconductor manufacturing requirements and have a dielectric constant less than 2. During the last decade, however, nanoporous media made of polymer [2,3] and SiO_2 [4–9] have been identified as potential solutions. In this approach, nano-size air bubbles ($\epsilon_r = 1.0$) are incorporated into a continuous matrix thus, reducing the effective dielectric constant of the nanoporous material. Then, the specific effective dielectric constant is tailored by varying the porosity.

In a similar manner, nanoporous silicon and SiO_2 have been used to manufacture waveguides [9–11], Bragg reflectors [12–18], Fabry-Perot filters [12,14,16,17,19], and antireflection coatings [20,21]. For example, in order to confine and propagate electromagnetic (EM) radiation within a waveguide, the guide region itself must have a higher index of refraction than the surrounding cladding [22]. Moreover, Bragg reflectors and Fabry-Perot filters are built by generating alternating layers with prescribed thickness and index of refraction. This geometry takes advantage

---

* Corresponding author. Tel.: +1 310 206 5598; fax: +1 310 206 2302.
E-mail address: pilon@seas.ucla.edu (M.M. Braun).

0040-6090/$ - see front matter © 2005 Elsevier B.V. All rights reserved.
doi:10.1016/j.tsf.2005.08.173

of constructive and destructive interferences to selectively reflect or transmit at desired wavelengths. Destructive interferences are also used by simple quarter-wave antireflection coatings to reduce or eliminate reflection from a surface. The effect is optimized by utilizing a coating material with index of refraction equal to the geometric mean of the two surrounding indices [22]. In all of these optical applications, the use of nanoporous media enables tuning of the index of refraction by simply controlling the morphology and porosity of the nanosize voids.

In order to design a material with the desired properties one needs to understand and predict the effect of the pores (shape, size, and concentration) on the properties of the host medium. This paper aims at understanding and quantifying these effects. First, the various models commonly used in the literature are reviewed. Then, numerical simulations of EM wave transport in non-absorbing nanoporous media are presented. Finally, comparisons with effective property models are discussed.

2. Current state of knowledge

Effective medium models treat heterogeneous media as homogeneous media with some effective properties. However, there are no explicit criteria as for when this approach is valid. The rule of thumb stating that the overall characteristic length L of the system should be much larger than the average pore diameter D has been used extensively. Typically, one uses the criteria $L \geq 10D$. Unfortunately, this rule seems to be arbitrary and is not supported by any rigorous analysis. Moreover, numerous effective media models have been suggested including (1) the Maxwell-Garnett Theory, (2) the Bruggeman effective medium approximation, (3) the parallel and (4) series models, (5) the reciprocity model, and (6) the models recently derived from the volume averaging method.

The Maxwell-Garnett Theory (MGT) [23] was first developed to model the effective electric permittivity of heterogeneous media consisting of *monodispersed* spheres arranged in a cubic lattice structure within a continuous matrix and of diameter much smaller than the wavelength of the incident EM wave. Then, the effective dielectric constant $\epsilon_{\mathrm{r,eff}}$ is expressed as,

$$\epsilon_{\mathrm{r,eff}} = \epsilon_{\mathrm{r,c}}\left[1 - \frac{3\phi\left(\epsilon_{\mathrm{r,c}} - \epsilon_{\mathrm{r,d}}\right)}{2\epsilon_{\mathrm{r,c}} + \epsilon_{\mathrm{r,d}} + \phi\left(\epsilon_{\mathrm{r,c}} - \epsilon_{\mathrm{r,d}}\right)}\right] \tag{1}$$

where $\epsilon_{\mathrm{r,c}}$ and $\epsilon_{\mathrm{r,d}}$ are the dielectric constant of the continuous and dispersed phases, respectively, while ϕ is the porosity. The MGT is not valid over the entire range of porosities since the spheres start overlapping for porosity values of $\pi/6 \simeq 52\%$ for a 3D cubic lattice arrangement.

To address this issue, Bruggeman [24] considered a similar situation of *polydispersed* spheres distributed in a continuous medium. The effective dielectric constant $\epsilon_{\mathrm{r,eff}}$ is obtained by solving the following implicit equation,

$$1 - \phi = \frac{\left(\dfrac{\epsilon_{\mathrm{r,eff}}}{\epsilon_{\mathrm{r,c}}} - \dfrac{\epsilon_{\mathrm{r,d}}}{\epsilon_{\mathrm{r,c}}}\right)}{\left[\left(\dfrac{\epsilon_{\mathrm{r,eff}}}{\epsilon_{\mathrm{r,c}}}\right)^{1/3}\left(1 - \dfrac{\epsilon_{\mathrm{r,d}}}{\epsilon_{\mathrm{r,c}}}\right)\right]} \tag{2}$$

Despite applicability to the full range of porosity ($0 \leq \phi \leq 1$), the Bruggeman model is not used as often as the MGT in the literature [25].

Other commonly encountered models are the parallel and series models which have been used, for example, for the effective dielectric constant, index of refraction, as well as thermal and electrical conductivities. The parallel model gives the effective property ψ_{eff} as a linear function of the properties of the continuous and dispersed phases, i.e.,

$$\psi_{\mathrm{eff}} = (1 - \phi)\psi_{\mathrm{c}} + \phi\psi_{\mathrm{d}} \tag{3}$$

The series model on the other hand, gives

$$\frac{1}{\psi_{\mathrm{eff}}} = \frac{1 - \phi}{\psi_{\mathrm{c}}} + \frac{\phi}{\psi_{\mathrm{d}}} \tag{4}$$

Alternatively, del Rio et al. [26] suggested the following effective model for electrical conductivity based on the reciprocity theorem,

$$\sigma_{\mathrm{eff}} = \sigma_{\mathrm{c}}\frac{1 + \phi\left(\sqrt{\sigma_{\mathrm{c}}/\sigma_{\mathrm{d}}} - 1\right)}{1 + \phi\left(\sqrt{\sigma_{\mathrm{d}}/\sigma_{\mathrm{c}}} - 1\right)} \tag{5}$$

The authors successfully validated this model against experimental data for the electrical conductivity of several binary metallic mixtures.

A more rigorous approach, albeit more mathematically involved, was recently derived [27–29] by applying the volume averaging theory (VAT) to the Maxwell's equations. Models were proposed for the effective dielectric constant $\epsilon_{\mathrm{r,eff}}$ and relative permeability $\mu_{\mathrm{r,eff}}$ of a two-phase mixture as,

$$\epsilon_{\mathrm{r,eff}} = (1 - \phi)\epsilon_{\mathrm{r,c}} + \phi\epsilon_{\mathrm{r,d}} \quad \text{and}$$
$$1/\mu_{\mathrm{r,eff}} = (1 - \phi)/\mu_{\mathrm{r,c}} + \phi/\mu_{\mathrm{r,d}}. \tag{6}$$

The range of validity of these expressions was discussed in depth, and a set of inequalities to be satisfied was developed. The authors conclude that "the constraints [posed by these inequalities] are very severe and are not satisfied for many processes". Note also that Eq. (6) does not satisfy the reciprocity theorem [26,30]. This can be attributed to the fact that the reciprocity theorem applies to irrotational vector fields [30]. However, in electromagnetic wave propagation, the curl of the electric and magnetic fields are non-zero as the time-dependent fields are coupled through Faraday's law of induction and Ampere's law.

Moreover, all the above models disregard the shape, the size distribution, and the spatial distribution of the pores.

However, these characteristics were stated to affect the effective properties of the heterogeneous medium [2,3]. Attempts have been made to account for non-spherical cell geometry by modifying the Maxwell-Garnett [31] and the Bruggeman [32,33] models. For example, Schultz [33] generalized the Bruggeman model for dispersions of randomly oriented spheroids. This model also accounts for the orientation of the cells by incorporating the angle between the revolution axis of the spheroid and the incident energy direction. Similarly, Robles et al. [30] proposed a model for randomly distributed and oriented elliptical inclusions using the reciprocity theorem and accounting for possible overlapping. Models such as these are difficult to use in practice because they are involved and/or require specific knowledge of the shape and orientation of the cells.

Finally, note that the above models have been used to predict properties for which they were not necessarily derived. For example, the MGT developed for the electric permittivity has been used for the index of refraction [34,35]. Overall, it is not always clear to the user which model is the most appropriate in any particular situation. Experimental data could be used to evaluate the various models, however the conclusions drawn can be contradictory [36]. For example, Si et al. [7] concluded that the series model best describes the dielectric constant of nanoporous silica thin films with uniformly distributed closed voids. Krause et al. [3], on the other hand, concluded that the Maxwell-Garnett model is more appropriate for polymeric closed-cell nanofoam. This apparent contradiction may be attributed to the difficulties and uncertainties in measuring the film porosity, the pore size and shape, and also the optical properties of a nanoporous thin film. To address this issue, the present study aims at numerically simulating EM wave transport in non-absorbing nanoporous media in order to determine (1) the range of validity of the effective medium approach and (2) the most appropriate effective property model for the dielectric constant and for the index of refraction of non-absorbing nanoporous media.

3. Analysis

3.1. Index of refraction from the volume averaging theory

A dielectric but non-magnetic material is characterized by its *real* dielectric constant ϵ_r and its *real* index of refraction n such that $n=\sqrt{\epsilon_r}$. Then, recasting the dielectric constants of the continuous and dispersed phases in terms of their indices of refraction, i.e. $\epsilon_{r,c}=n_c^2$ and $\epsilon_{r,d}=n_d^2$, the VAT model for $\epsilon_{r,eff}$ given by Eq. (6) can be rewritten for the effective index of refraction as,

$$n_{eff}=\sqrt{\epsilon_{r,eff}}=\sqrt{(1-\phi)n_c^2+\phi n_d^2}. \tag{7}$$

This relationship can be extended to semi-conductor materials at wavelengths at which they do not absorb.

3.2. Governing equations and numerical implementation

In order to develop the numerical model, let us first consider a surrounding environment (medium 1, n_1) and a non-absorbing dense thin film (medium 2, n_2) deposited onto a non-absorbing dense substrate (medium 3, n_3). A linearly polarized plane wave in transverse electric mode (TE mode) is incident normal to the film top surface and propagates through the two-dimensional thin film along the x-direction (see Fig. 1). As the wave propagates in the $x-y$ plane, it has only one electric field component in the z-direction, while the magnetic field has two components in the $x-y$ plane (i.e. perpendicularly polarized), such that in a general time-harmonic form,

$$\vec{E}(x,y,t)=E_z(x,y)e^{i\omega t}\vec{e_z} \tag{8}$$

and

$$\vec{H}(x,y,t)=\left[H_x(x,y)\vec{e_x}+H_y(x,y)\vec{e_y}\right]e^{i\omega t}. \tag{9}$$

Here, $\vec{E}$ is the electric field vector, $\vec{H}$ is the magnetic field vector, and $\omega=2\pi c_0/\lambda$ is the angular frequency of the wave.

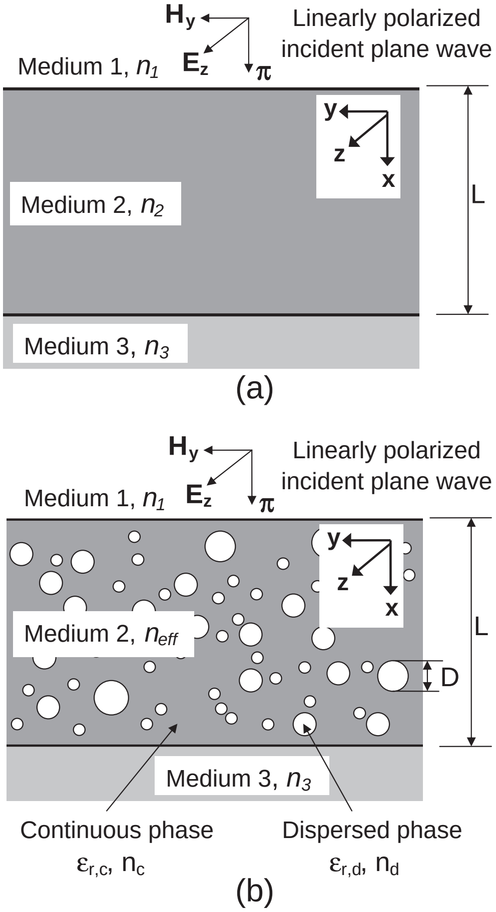

Fig. 1. Schematic of two-dimensional (a) dense and (b) closed-cell nanoporous thin-film exposed to a linearly polarized plane wave.

The unit vectors for the Cartesian coordinate system are $\vec{e_x}$, $\vec{e_y}$ and $\vec{e_z}$. For general time-varying fields in a non-conducting medium, Maxwell's equations can be written as

$$\frac{1}{\mu_r\mu_0}\nabla\times\left[\nabla\times\vec{E}(x,y,t)\right]-\omega^2\epsilon_r\epsilon_0\vec{E}(x,y,t)=0 \tag{10}$$

$$\frac{1}{\varepsilon_r\varepsilon_0}\nabla\times\left[\nabla\times\vec{H}(x,y,t)\right]-\omega^2\mu_r\mu_0\vec{H}(x,y,t)=0 \tag{11}$$

where μ_0 and μ_r are the magnetic permeability of vacuum and the relative magnetic permeability, respectively. The associated boundary conditions are

$$\vec{n}\times\left(\vec{H}_1-\vec{H}_2\right)=\vec{0} \quad \text{at the surroundings} - \text{film interface} \tag{12}$$

$$\vec{n}\times\vec{H}=\vec{0} \qquad \text{at the symmetry boundaries} \tag{13}$$

$$\mu_0^{1/2}\left(\vec{n}\times\vec{H}\right)+n_2\epsilon_0^{1/2}\vec{E}=\vec{0}$$
$$\text{at the film} - \text{subtrate interface} \tag{14}$$

$$\mu_1^{1/2}\left(\vec{n}\times\vec{H}\right)+n_1\epsilon_0^{1/2}\vec{E}=2n_1\epsilon_0^{1/2}\vec{E_0}$$
$$\text{at the source surface} \tag{15}$$

where $\vec{n}$ is the normal vector to the appropriate interface. Eq. (14) corresponds to a semi-infinite substrate while Eq. (15) models the source surface from which the incident EM wave $\vec{E_0}$ is emitted, but that will be transparent to the reflected waves.

Moreover, the Poynting vector $\vec{\pi}$ is defined as the cross product of the electric and magnetic field vectors, i.e. $\vec{\pi}=\vec{E}\times\vec{H}$. Its magnitude corresponds to the energy flux carried by the propagating EM wave. Solving Maxwell's equations for the nonzero component of the electric field vector E_z, and relating it to the magnetic field gives

$$H_y=\frac{n}{\mu_r\mu_0c_0}E_z. \tag{16}$$

Averaging the Poynting vector over an appropriate time interval yields [22],

$$|\pi|_{\text{avg}}=\frac{n}{2\mu_r\mu_0c_0}E_z^2. \tag{17}$$

The incident electric field E_z and therefore the incident time-averaged Poynting vector $|\pi_0|_{\text{avg}}$ are imposed at all locations along the source surface. The values of the Poynting vector along the film-substrate interface are then calculated numerically and averaged along the boundary to yield $|\pi_t|_{\text{avg}}$. The transmittance of the thin film is then recovered by taking the ratio of the transmitted to incident values, $T_{\text{film}}=|\pi_t|_{\text{avg}}/|\pi_0|_{\text{avg}}$. Similarly, the magnitude of the reflected time-averaged Poynting vector $|\pi_r|_{\text{avg}}$ is computed numerically, and the reflectance of the film is computed according to $R_{\text{film}}=|\pi_r|_{\text{avg}}/|\pi_0|_{\text{avg}}$. Finally, the above equations were solved numerically using a commercially available finite element solver applying the Galerkin finite element method on unstructured meshes. The two-dimensional Maxwell's equations are solved in the frequency domain using a 2D transverse electric (TE) wave formulation as described by Eq. (8). In particular, discretization uses second order elements to solve for the electric field. In order to validate the numerical implementation of the equations and boundary conditions, the interference pattern of a dense and non-absorbing thin film of SiO_2 with thickness L and index of refraction n_2 deposited on a silicon substrate with index of refraction n_3 and subject to normal incident light of variable wavelength λ was simulated. Numerical results fall within rounding error on the sixth recorded significant digit of the well-known analytical solution expressing the transmissivity and reflectivity as a function of the product n_2L/λ [22, p. 140].

3.3. Simulations of nanoporous thin films

Fig. 1b shows a schematic of a nanoporous thin film on a semi-infinite substrate. The heterogeneous medium is assumed to be axisymmetric and isotropic with randomly distributed pores which can be modelled as a two-dimensional structure. Moreover, all interfaces were treated as optically smooth. As the EM wave travels through the nanoporous thin film, interferences and scattering take place. However, scattering can be neglected if the size of the individual inhomogeneities dispersed in an otherwise homogeneous matrix is much smaller than the wavelength of the incident radiation [28,37]. A quantitative criteria requires that the size parameter $\chi=\pi D/\lambda$ be much smaller than unity, where D is the pore diameter (or an equivalent) and λ is the incident wavelength [38]. In the present study χ varies between 0.0023 and 0.23, and the fraction of energy scattered by pores of various shape and size was neglected relative to that transmitted and reflected by the film in the incident direction. This assumption was confirmed numerically by comparing the magnitude of the y-component of the Poynting vector perpendicular to the incident directions with its x-component at all locations in the x–y plane. For $\chi=0.23$, the maximum value of the y-component of the Poynting vector was conservatively estimated to be less than 0.5% of the minimum x-component. For the smaller pore sizes this value was several orders of magnitude smaller (0.05% for $\chi=0.023$ and negligibly small for $\chi=0.0023$). Similarly, polarization effects are disregarded since (1) the incident EM wave is normal to the surface, i.e., the plane of incidence is not defined and the components of the polarization cannot be distinguished [22], (2) scattering is neglected, and (3) we assume the heterogeneous medium to be axisymmetric and isotropic. In addition, non-linear optical effects are neglected. Finally, surface phonon and plasmon polaritons are not observed in the current situation as resonance modes were not excited for the materials and wavelengths considered.

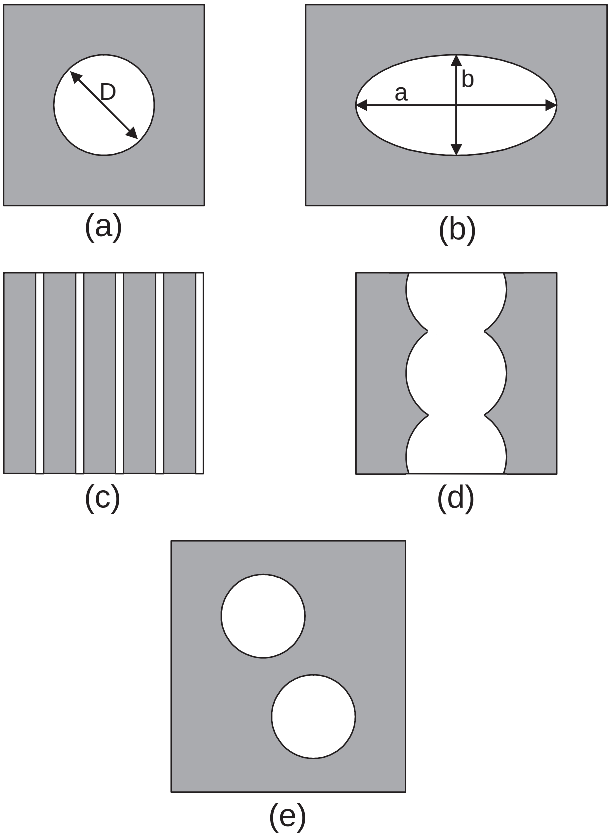

Fig. 2. Geometry of the various unit cells investigated.

The geometry was further simplified for numerical simulations by building a simple 2D unit cell consisting of domains of dispersed phase embedded in a matrix as shown in Fig. 2. Multiple cells were then added on top of each other to simulate nanoporous thin films of various thicknesses but identical porosities. This results in a regular periodic structure similar to those used in simulations of photonic band gap crystals. However, all cases in the current study are outside of the zero transmission bands for the wavelengths considered [39]. The surrounding environment and the dispersed phase were treated as vacuum ($n_1 = n_d = 1$). Silicon dioxide was used as the thin film continuous phase characterized by a real index of refraction equal to $n_c = 1.4442$ at 1.55 μm [40]. The silicon substrate is weakly absorbing about this wavelength with an absorption index k_3 less than 1.5×10^{-6} [22]. Therefore, as a first order approximation, the silicon substrate was modelled as non-absorbing with an index of refraction $n_3 = 3.48$. Moreover, the wavelength of 1.55 μm was chosen because of its predominant use in the telecommunication industry, and ready production by AlGaAs semiconductor laser diodes.

The Maxwell's equations are solved numerically to simulate the EM wave transport in each phase of the nanoporous thin films. Eq. (12) is used as the boundary condition not only at the vacuum-film interface but also at the SiO_2–pore interfaces. It is important to note that Maxwell's equations are generally applied to macroscopic averages of the fields which can vary widely in the vicinity of individual atoms where they undergo quantum mechanical effects. These effects are neglected in the present study and all phases are treated as homogeneous and isotropic media for which dielectric constants ϵ_r and indices of refraction n are defined. This is a reasonable assumption for length scales on the order of ten lattice constants, or about 5 nm [41, p. 387].

Fig. 3 is a schematic representation of a model consisting of three unit cells with $\phi = 19.63\%$. It indicates material properties of the various domains and the locations at which each of the boundary conditions are applied. To ensure proper application of the symmetry boundary condition, a 10×10 and a 10×1 unit cell arrangement were modelled. In both cases, the average transmittance and reflectance were identical. Thus, one-unit-cell-wide models are used in all other cases so as to reduce computational time.

Finally, the computed local transmitted Poynting vector is averaged along the film-substrate interface for calculating the film transmittance, T_{film}. The local transmitted energy flux varies slightly as a function of position for the nanoporous geometries considered in this study. For example, the relative difference between the local and averaged transmittance along the nanoporous film/substrate interface for several film thicknesses and constant porosity $\phi = 19.63\%$ is less than 1% in the case of spherical pores 100 nm in diameter, 0.01% for 10 nm, and negligibly small for 1 nm.

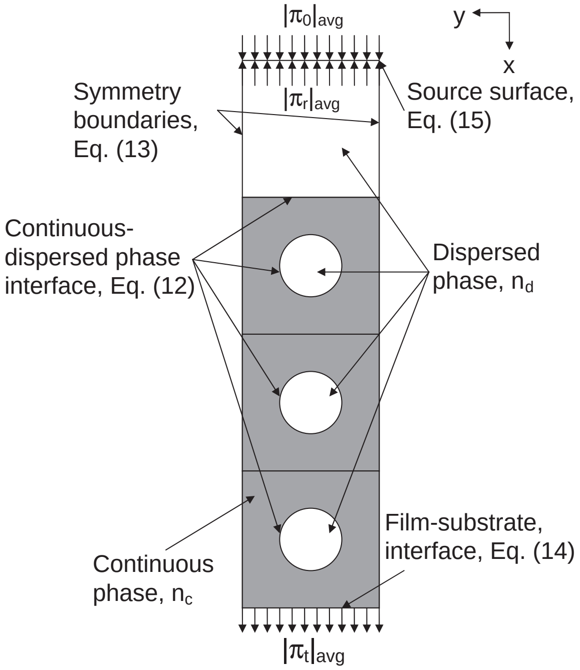

Fig. 3. Schematic of model composed of three unit cells. Each contains a centered pore and has porosity 19.63%. The schematic also depicts where boundary conditions and domain properties are assigned.

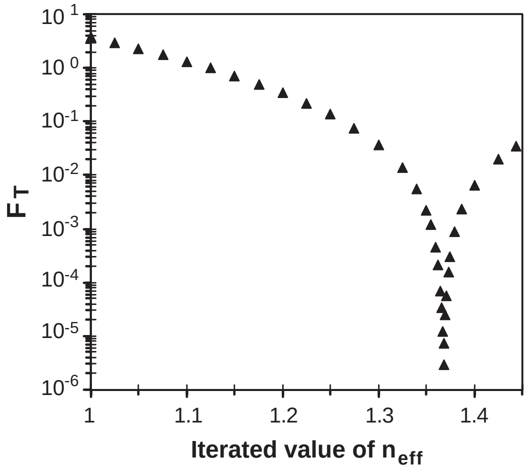

Fig. 4. Error as calculated according to Eq. (22) versus effective index of refraction n_{eff}.

3.4. Recovery of the effective index of refraction

Numerous methods have been proposed for determining the film thickness and the real and imaginary components of the complex index of refraction from reflectance and transmittance data [42–48]. In the present study, this process is greatly simplified because the absorption coefficient vanishes for both phases and the film thickness is known. Then, the system of equations valid for a non-absorbing homogeneous media on a substrate under *normal incidence* and accounting for interferences is [22],

$$T_{\text{film}} = \frac{n_3 t_{12}^2 t_{23}^2}{1 + r_{12}^2 r_{23}^2 + 2 r_{12} r_{23} \cos 2\beta} \tag{18}$$

$$R_{\text{film}} = \frac{r_{12}^2 + r_{23}^2 + 2 r_{12} r_{23} \cos 2\beta}{1 + r_{12}^2 r_{23}^2 + 2 r_{12} r_{23} \cos 2\beta} \tag{19}$$

where

$$r_{12} = \frac{1 - n_{\text{eff}}}{1 + n_{\text{eff}}}, t_{12} = \frac{2}{1 + n_{\text{eff}}}, \\ r_{23} = \frac{n_{\text{eff}} - n_3}{n_{\text{eff}} + n_3}, t_{23} = \frac{2 n_{\text{eff}}}{n_{\text{eff}} + n_3} \tag{20}$$

and

$$\beta = \frac{2\pi n_{\text{eff}} L}{\lambda} \tag{21}$$

Here, n_{eff} is the effective index of refraction of the nanoporous film, n_3 is the index of refraction of the silicon substrate, and T_{film} and R_{film} are the transmittance and reflectance, respectively. Eq. (20) gives the Fresnel coefficients for non-absorbing media where medium 1 has index of refraction n_1 equal to 1. Finally, β is the phase difference in the wave of incident wavelength λ after one pass through the film of thickness L.

In the present study, the Maxwell's equations are solved numerically and the transmittance T_{film} computed for 201 values of λ in the spectral interval from 1.05 to 2.05 μm. The analytical solution for the transmittance T_{film} is also calculated using Eqs. (18)–(21) for an arbitrary value of n_{eff}. The quadratic relative differences between the numerical and analytical values of the transmittance are then computed at each wavelength and summed according to

$$F_{\text{T}} = \sum_{i=1}^{201} \left(T_{\text{film,A},i} - T_{\text{film,N},i} \right)^2 \tag{22}$$

where the subscripts N and A denote numerical and analytical values, respectively. Then, an iterative procedure is followed so as to identify the value of n_{eff} that minimizes the difference F_{T}. Fig. 4 shows the evolution of F_{T} as a function of the guessed value n_{eff} for a 400-nm-thick SiO_2 thin film with 10 nm pores and 19.63% porosity. It clearly shows that the error reaches a minimum in the interval of possible solutions bounded by the indices of refraction of the dispersed and continuous phase, since a priori n_{eff} should fall between $n_{\text{d}}=1$ and $n_{\text{c}}=1.4442$.

4. Results and discussion

The numerical simulations performed explore (i) the effect of the film thickness and the validity of the effective medium approach, (ii) the effect of pore shape, (iii) the effect of the pore spatial distribution, and (iv) the effect of the overall film porosity on the refraction index of non-absorbing nanoporous thin films.

4.1. Effect of film thickness

Fig. 5 shows the evolution of the retrieved index of refraction as a function of the ratio of the film thickness L to the diameter of the spherical pores D for a film with 19.63%

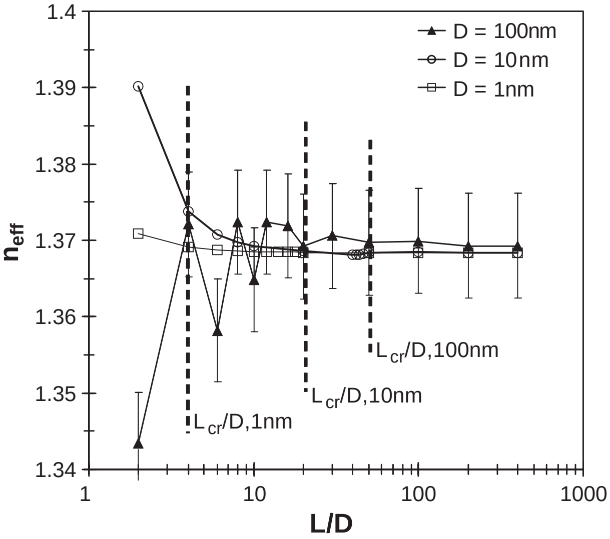

Fig. 5. Evolution of effective index of refraction as a function of L/D for films with 19.63% porosity and three different pore diameters.

porosity and three different pore diameters equal to 1, 10, and 100 nm. For each data set, only the film thickness L is varied by varying the number of unit cells stacked in the layer. Then, several conclusions can be drawn:

1. For any given pore diameter D and small values of film thickness L, the effective index of refraction is a function of L and D. Therefore the effective medium approach is not valid.
2. Beyond a critical thickness L_{cr}, the effective medium approach is valid and an effective index of refraction can be defined as a function of porosity ϕ and of the constituent phase indices of refraction n_c and n_d only.
3. The magnitude of the critical film thickness L_{cr} is a function of the pore diameter and the incident radiation wavelength λ. In Fig. 5, the L_{cr}/D values are arbitrarily defined so that all subsequent values of n_{eff} fall within 0.05% of the converged solution. In the present case, L_{cr} is found to be up to 50 times the pore diameter for 100 nm pores.

4.2. Effect of pore shape

Several experimental studies of nanoporous media have concluded that flattened cells affect the effective dielectric constant and index of refraction of the medium [2,3]. To explore this question, simulations were performed for various pore shapes including elliptical pores, overlapping spherical pores, and columnar pores. Also, this resulted in simulations of both open and closed-cell nanoporous structures.

First, elliptical pores characterized by thickness b and width a, as depicted in Fig. 2b, are considered. The porosity was varied by changing the length and width of the unit cell. The degree of scattering was found to be negligible in most cases by comparing the magnitude of the x- and y-components of the Poynting vector at all locations in the computational domain. When it was not deemed negligible, the uncertainty due to scattering was calculated and considered when determining the critical thickness L_{cr}. First, two values (1 and 10 nm) of the parameter b were considered while maintaining a constant ratio $a/b=2$ and porosity $\phi=19.63\%$. As in the case of spherical pores, variations in the effective properties are observed for low values of L/b, and a single value is reached for larger values of L/b, as shown in Fig. 6. Additionally, cases were computed this time with $b=10$ nm, and $a/b=1/6$, 2, 6, and 12 at various porosities (not shown). In all cases, the converged effective properties were equal to those found using spherical pores ($a/b=1$) with the same porosity.

Moreover, in order to simulate porous silicon, which features open-cell morphology, simulations were performed for geometries consisting of columnar pores, as shown in Fig. 2c. The same value of the index of refraction was retrieved for all film thicknesses, i.e., the effective medium approximation is valid for all film thicknesses. In addition, the retrieved value of n_{eff} was identical to that for nanoporous thin film of equal porosity but containing spherical or elliptical pores.

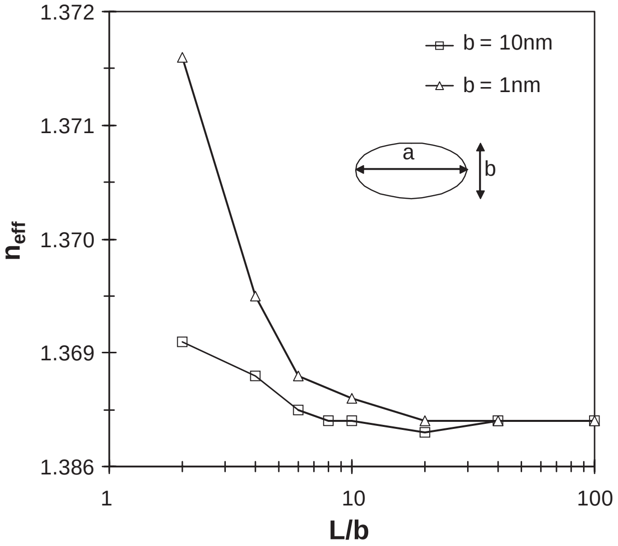

Fig. 6. Evolution of effective index of refraction as a function of L/D for elliptical pores with aspect ratio $a/b=2$ and $b=1$ and 10 nm for an overall porosity of $\phi=19.63\%$.

An open-cell morphology intended to represent overlapping spherical pores, such as those found in aerogels, was also simulated (see Fig. 2d). The same effective index of refraction was retrieved for all thicknesses; its value was equal to that found for all other pore shapes and nanoporous thin films of identical porosity.

Another simulated pore geometry included two staggered spherical pores per unit cell as illustrated in Fig. 2e. Once again, it was found that the effective index of refraction converged to the same value as that of the previously considered morphologies with identical porosity.

Finally, fluctuations in the value of n_{eff} for small values of L/D are caused by interferences due to reflections off the interfaces perpendicularly oriented to the direction of wave propagation. Beyond L_{cr} this effect averages out, and a constant value of n_{eff} is displayed. This is first demonstrated by the lack of variation seen in n_{eff} for the simulations of open-cell geometries depicted in Fig. 2c and d. These geometries have no internal surfaces from which waves can reflect, thus inhibiting the interference effect. As a result, the retrieved n_{eff} is constant for all film thicknesses. For closed pores, however, the fluctuation in the retrieved index of refraction as a function of film thickness increases significantly as the pore diameter increases. This phenomenon can be explained simply by considering the length scales of the films relative to the wavelength of the incident radiation. For example, for spherical pores with $D=1$, 10, and 100 nm, L_{cr} can be found to be approximately 10 nm, 600 nm, and 30 μm, respectively, for an incident radiation wavelength of 1.55 μm (Fig. 5). In the case of 1 nm pore size, the phase difference β between interfering waves is negligibly small. In the case of the 100-nm pore size, however, the phase

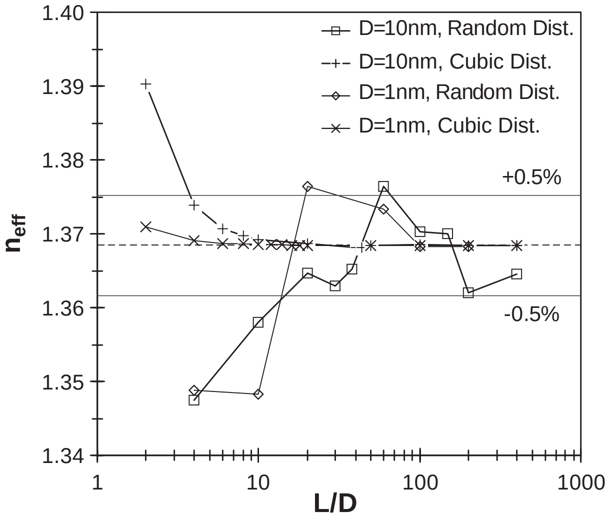

Fig. 7. Evolution of effective index of refraction as a function of L/D for regular and random pore distribution and porosity $\phi=19.63\%$.

difference is larger and responsible for the large fluctuations in n_{eff} versus L/D as illustrated in Fig. 5. Thus, the critical thickness L_{cr}, beyond which the effective medium approach is valid, depends also on the wavelength λ.

4.3. Effect of pore spatial arrangement

Thus far, all simulations were performed on models built from basic unit cells. To explore a situation where the pores are not arranged in a regular cubic distribution, several simulations were performed on films of varying thickness with pores distributed at random locations between 0 and L along the x-axis. Values that would have resulted in overlapping pores were eliminated so as to maintain a closed-cell structure. Cases with pores' diameters of 1 and 10 nm were simulated. Fig. 7 compares the evolution of the effective index of refraction as a function of L/D for randomly located pores and that for regular cubic pore distribution while maintaining constant porosity ($\phi=$ 19.63%). Larger values of L_{cr} are obtained for each pore diameter in the cases of randomly distributed pores. However, beyond L_{cr} the retrieved effective index of refraction is the same as that found using previously discussed pore morphologies of equal porosity. The 1 nm pore case is fully converged to this value at $L_{\mathrm{cr}}/D=100$, and the 10 nm case is within 0.5% at $L/D=200$.

4.4. Effect of porosity

From the above analysis, one can conclude that beyond a critical thickness, the effective medium approach is valid and the effective index of refraction depends only on the porosity and index of refraction of each of the two constituent phases, but not on the pore shape, size distribution, or spatial distribution. This confirms the general form of commonly used effective medium models such that $n_{\mathrm{eff}}=f(\phi, n_{\mathrm{c}}, n_{\mathrm{d}})$ (see Eqs. (1)–(6)).

To assess the validity of the commonly used models, simulations were run for silicon dioxide with 10 nm spherical closed pores, and for porous silicon with columnar pores. For silicon, the incident wavelength was chosen to be $\lambda=2.71$ μm at which the complex index of refraction is $m_{\mathrm{Si}}=3.44-i2.5\times10^{-9}$ [22]. Thus, the absorption coefficient can also safely be neglected. Fig. 8 shows the converged values of the effective index of refraction plotted versus porosity along with predictions of the above-discussed models. The Bruggeman model differed from the MGT model by a maximum of only 2.3% for silicon, and by only 0.1% for SiO_2. Thus, the Bruggeman model will not be discussed further.

The numerical values retrieved for n_{eff} match those predicted by the volume averaging technique [Eq. (7)]

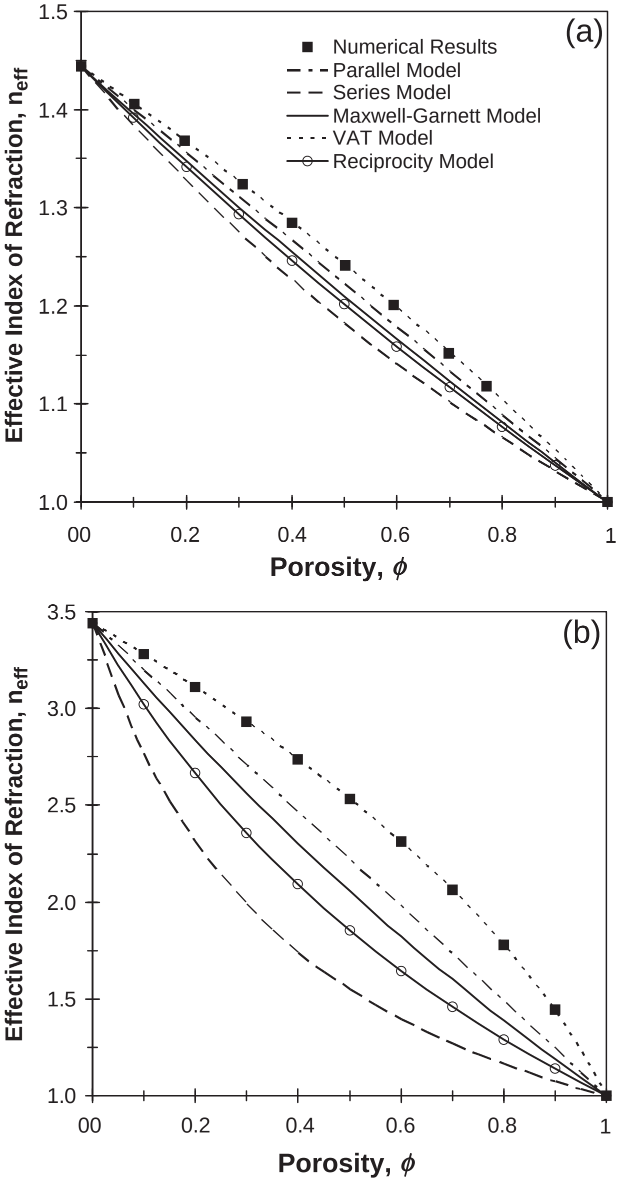

Fig. 8. Numerical result for effective index of refraction as a function of porosity for (a) nanoporous SiO_2 at $\lambda=1.55$ μm and (b) nanoporous Si at $\lambda=2.71$ μm.

within rounding error. The relative difference between the parallel, Maxwell-Garnett, reciprocity, and series models and the numerical results for nanoporous SiO_2 was up to 1.7%, 2.6%, 3.3%, and 4.9%, respectively. In the case of porous silicon, these differences are larger and can reach up to 16.4%, 22.4%, 29.3%, and 39.5%, respectively. Therefore, as the index of refraction of the continuous phase material increases, the percent difference between the various effective medium models and the numerically predicted value of n_{eff} increases.

Moreover, simulations were also conducted to investigate a hypothetical medium in which the dispersed phase has a larger index of refraction than the continuous phase. Specifically, the supposed case of spherical silicon particles ($n_{\text{d}}=3.44$) distributed in an otherwise continuous SiO_2 matrix ($n_{\text{c}}=1.426$) was considered. The incident wavelength was chosen as 2.71 μm such that both phases could be considered as non-absorbing. As in the previous cases, the effective index of refraction initially varied for relatively thin films before converging to a value equal to that predicted by the VAT model. Note that here, the effective index of refraction increases with porosity since $n_{\text{d}}>n_{\text{c}}$.

Finally, the conditions for the validity of the VAT model proposed by del Rio and Whitaker [27,28] based on order of magnitude estimates seem to be too stringent [36]. Indeed, even though these conditions are not satisfied, the predictions of the VAT model for the effective properties compare very well with those computed from numerical results.

5. Conclusions

Numerous effective medium models have been proposed and used in the literature. However, it remained unclear which model is applicable to a specific situation. In order to address this issue, numerical solutions of the Maxwell's equations for axisymmetric nanoporous thin films of various porosity and with open and closed pores of various shape, size, and spatial distribution have been presented and discussed. Several conclusions can be drawn.

First, there exists a critical nanoporous film thickness L_{cr} below which the effective index of refraction is a function of (i) the film thickness, (ii) the pore shape, (iii) their size, (iv) their spatial distribution, and (v) the wavelength considered. For film thickness less than L_{cr}, the effective medium approach is not applicable and the heterogeneous nature of the medium should be taken into account.

For films thicker than the critical thickness L_{cr}, the effective medium approach is valid and an effective index of refraction can be defined only as a function of porosity ϕ and of the indices of refraction of the constituent phases, n_{c} and n_{d}. In other words, *the pore shape, size, and spatial distribution have no effect on the effective index of refraction of the nanoporous medium*.

Unfortunately, it was not possible to find a simple correlation between the critical thickness L_{cr} and the pore shape, size, spatial distribution, or the wavelength considered. Qualitatively, for randomly distributed pores, L_{cr} increases as the pore size increases.

Finally, the models obtained from the VAT are recommended for calculating the effective index of refraction and the effective dielectric constant of the two-phase non-absorbing nanoporous media when the effective medium approximation is valid ($L>L_{\text{cr}}$). Then,

$$n_{\text{eff}} = \sqrt{(1-\phi)n_{\text{c}}^2 + \phi n_{\text{d}}^2}$$
$$\epsilon_{\text{r,eff}} = (1-\phi)\epsilon_{\text{r,c}} + \phi\epsilon_{\text{r,d}}. \tag{23}$$

Practically, models other than the VAT model give acceptable predictions when the continuous and dispersed phases have similar indices of refraction. However, the predictions can be significantly erroneous for nanoporous media when one of the constituting phases features an index of refraction significantly different from the other.

The discrepancies between the different models and reported experimental data for $\epsilon_{\text{r,eff}}$ and n_{eff} can be attributed to (1) the fact that the film thickness was smaller than L_{cr} such that the effective medium approach is not valid, and (2) experimental uncertainty associated with the porosity ϕ and with the properties of the continuous phase. Uncertainty in these values could result in significant error in the model predictions. Together, these effects could lead to erroneous and often contradictory conclusions about the effect of the size and shape of the pores on the effective optical properties of nanoporous media.

Nomenclature

a	ellipse dimension parallel to incident radiation
b	ellipse dimension perpendicular to incident radiation
C	electrical capacitance
c	speed of light
D	pore diameter
$\vec{E}$	electric field vector
$\vec{H}$	magnetic field vector
k	absorption index
L	thickness of a thin film
m	complex index of refraction
n	real part of the complex index of refraction
$\vec{n}$	normal vector to interface
r	Fresnel reflection coefficient
R	electrical resistance or reflectance
t	Fresnel transmission coefficient
T	transmittance

Greek symbols

β	phase difference between interfering waves
χ	scattering size parameter
ϵ	electric permittivity
ϕ	porosity
λ	wavelength of the electromagnetic wave
μ	magnetic permeability

$\vec{\pi}$	Poynting vector
ω	angular frequency of electromagnetic wave
ψ	general property

Subscripts

0	refers to vacuum, or an incident property
1, 2, 3	refers to surrounding air, thin film, and substrate, respectively
A	refers to analytically attained value
avg	refers to time-averaged value
c	refers to continuous phase
cr	refers to critical value of L
d	refers to dispersed phase
eff	refers to effective properties
film	refers to thin film
N	refers to numerically attained value
r	refers to relative property, e.g. relative permittivity (dielectric constant)
r	refers to reflected Poynting vector
t	refers to transmitted Poynting vector
x	refers to x-direction
y	refers to y-direction
z	refers to z-direction

Acknowledgements

The authors would like to thank the Femlab support team for their valuable support in performing the numerical simulations. Thanks are also extended to Dr. Stéphane Durant for useful discussion and exchange of information. This work was supported in part by the National Science Foundation. L. Pilon acknowledges the support of NSF through the CAREER Award.

References

[1] B.Y. Tsui, C.C. Yang, K.L. Fang, IEEE Trans. Electron Devices 51 (1) (2004) 20.
[2] H.J. Cha, J. Hedrick, R.A. DiPietro, T. Blume, R. Beyers, D.Y. Yoon, Appl. Phys. Lett. 68 (14) (1996) 1930.
[3] B. Krause, G.H. Koops, N.F.A. van der Vegt, M. Wessling, M. Wubbenhorst, J. van Turnhout, Adv. Mater. 14 (15) (2002) 1041.
[4] H. Fan, H.R. Bently, K.R. Kathan, P. Clem, Y. Lu, C.J. Brinker, J. Non-Cryst. Solids 285 (2001) 79.
[5] C. Flannery, C. Murray, I. Streiter, W.E. Schulz, Thin Solid Films 388 (2001) 1.
[6] L.W. Hrubesh, L.E. Keene, V.R. Latorre, J. Mater. Res. 8 (7) (1993) 1736.
[7] J.J. Si, H. Ono, K. Uchida, S. Nozaki, H. Morisaki, N. Itoh, Appl. Phys. Lett. 79 (19) (2001) 3140.
[8] D.M. Smith, J. Anderson, C.C. Cho, G.P. Johnston, S.P. Jeng, Appl. Mater. Res. Soc. Symp. Proc. 381 (1995) 261.
[9] A. Jain, S. Rogojevic, S. Ponoth, I. Matthew, W.N. Gill, P. Persans, M. Tomozawa, J.L. Plawsky, E. Simonyi, Thin Solid Films 398 (2001) 513.
[10] A. Loni, L. Canham, M. Berger, R. Arens-Fischer, H. Munder, H. Luth, H. Arrand, T. Benson, Thin Solid Films 276 (1996) 143.
[11] H.F. Arrand, T.M. Benson, A. Loni, M.G. Krueger, M. Thoenissen, H. Lueth, Electron. Lett. 33 (20) (1997) 1724.
[12] M.G. Berger, M. Thonissen, R. Arens-Fischer, H. Munder, H. Luth, M. Arntzen, W. Thei, Thin Solid Films 255 (1995) 313.
[13] J. Diener, N. Künzner, D. Kovalev, E. Gross, V.Y. Timoshenko, G. Polisski, F. Koch, Appl. Phys. Lett. 78 (24) (2001) 3887.
[14] M. Krüger, M. Marso, M.G. Berger, M. Thönissen, S. Billat, R. Loo, W. Reetz, H. Lüth, S. Hilbrich, R. Arens-Fischer, P. Grosse, Thin Solid Films 297 (1997) 241.
[15] S. Zangooie, M. Schubert, C. Trimble, D. Thompson, J. Woollam, Appl. Opt. 40 (6) (2001) 906.
[16] S. Zangooie, R. Jansson, H. Arwin, J. Appl. Phys. 86 (2) (1999) 850.
[17] C. Mazzoleni, L. Pavesi, Appl. Phys. Lett. 67 (20) (1995) 2983.
[18] K. Kordás, S. Beke, A. Pap, A. Uusimaki, S. Leppävuori, Opt. Mater. 25 (2004) 257.
[19] A. Janshoff, K.P.S. Dancil, C. Steinem, E.P. Greiner, V.S.Y. Lin, C. Gurtner, K. Motesharei, M.J. Sailor, M.R. Ghadiri, J. Am. Chem. Soc. 120 (1998) 12108.
[20] I.M. Thomas, Appl. Opt. 31 (28) (1992) 6145.
[21] Q. Zhang, J. Wang, G. Wu, J. Shen, S. Buddhudu, Mater. Chem. Phys. 72 (2001) 56.
[22] M.Q. Brewster, Thermal Radiative Transfer and Properties, John Wiley and Sons, Inc., 1992.
[23] J.C.M. Garnett, Philos. Trans. R. Soc. London, Ser. A 203 (1904) 385.
[24] D.A.G. Bruggeman, Ann. Phys. (Leipz.) 24 (1935) 636.
[25] F. Cernuschi, S. Ahmaniemi, P. Vuoristo, T. Mantyla, J. Eur. Ceram. Soc. 24 (2004) 2657.
[26] J.A. del Rio, R.W. Zimmerman, R.A. Dawe, Solid State Commun. 106 (4) (1998) 183.
[27] J.A. del Rio, S. Whitaker, Trans. Por. Med. 39 (2000) 159.
[28] J.A. del Rio, S. Whitaker, Trans. Por. Med. 39 (2000) 259.
[29] V.S. Travkin, I. Catton, Adv. Heat Transf. 34 (2001) 1.
[30] M. Robles, J. Taguena-Martinez, J.A. del Rio, Thin Solid Films 293 (1997) 320.
[31] G. Grimvall, Thermophysical Preperties of Materials, Selected Topics in Solid State Physics, vol. XVIII, North-Holland Physics Publishing, 1986.
[32] R.E. Meredith, Studies in the conductivites of dispersions, Lawrence Radiation Laboratory Report, UCRL-8667, 1959.
[33] B. Schulz, High Temp. High Press. 13 (1981) 649.
[34] S. Labbe-Lavigne, S. Barret, F. Garet, L. Duvillaret, J. Coutaz, J. Appl. Phys. 83 (1998) 6007.
[35] C. Himcinschi, M. Friedrich, C. Murray, I. Streiter, S.E. Schulz, T. Gessner, D.R.T. Zahn, Semicond. Sci. Technol. 16 (11) (2001) 806.
[36] M. Braun, Effective optical properties of nanoporous thin films, Master's thesis, Department of Mechanical and Aerospace Engineering. University of California, Los Angeles, CA (2004).
[37] R. Viskanta, M.P. Mengüc„ Appl. Mech. Rev. 42 (9) (1989) 241.
[38] M.F. Modest, Radiative Heat Transfer, McGraw-Hill, New York, NY, 2002.
[39] S.G. Johnson, J.D. Joannopoulos, Photonic Crystals: The Road from Theory to Practice, Kluwer Academic Publishers, 2002.
[40] J.H. Wray, J.T. Neu, J. Opt. Soc. Am. 59 (6) (1969) 774.
[41] C. Kittel, Introduction to Solid State Physics, John Wiley and Sons, 1996.
[42] M.A. Khashan, A.M. El-Naggar, E. Shaddad, Opt. Commun. 178 (2000) 123.
[43] M.A. Khashan, A.M. El-Naggar, Opt. Commun. 174 (2000) 445.
[44] A.B. Djurisic, T. Fritz, K. Leo, Opt. Commun. 166 (1999) 35.
[45] J.C. Manifacier, J. Gasiot, J.P. Fillard, J. Phys. E: Sci. Instrum. 9 (1976) 1002.
[46] R. Swanepoel, J. Phys. E: Sci. Instrum. 16 (1983) 1214.
[47] J.J. Ruíz-Pérez, J.M. Gonzáles-Leal, D.A. Minkov, E. Márquez, J. Phys. D: Appl. Phys. 34 (2001) 2489.
[48] B.S. Richards, A. Lambertz, A.B. Sproul, Determination of the optical properties of non-uniformly thick non-hydrogenated sputtered silicon thin films on glass, Thin Solid Films 460 (2004) 247.